ACS OMEGA

Open Access

http://pubs.acs.org/journal/acsodf

Article

Spectral Splitting Solar Cells Consisting of a Mesoscopic Wide-Bandgap Perovskite Solar Cell and an Inverted Narrow-Bandgap Perovskite Solar Cell

Kei Ito, Kazuteru Nonomura, Ryota Kan, Keishi Tada, Ching Chang Lin, Takumi Kinoshita, Takeru Bessho, Satoshi Uchida,* and Hiroshi Segawa*

Cite This: *ACS Omega* 2024, 9, 3028−3034

Read Online

ACCESS | Metrics & More | Article Recommendations | Supporting Information

ABSTRACT: In comparison to monolithic perovskite/perovskite double-junction solar cells, a four-terminal spectrum-splitting system is a simple method to obtain a higher power conversion efficiency (PCE) because it has no constraints of unifying the structures of the top and bottom cells. In this work, utilizing the fact that low-bandgap Sn−Pb bottom cells work the best in p−i−n while Pb-based wide-bandgap top cells work better in an n−i−p architecture, a wide-bandgap (E_g = 1.61 eV) perovskite solar cell with a mesoscopic structure and a narrow-bandgap (E_g = 1.27 eV) perovskite solar cell with an inverted structure were combined to fabricate a double-junction four-terminal spectral splitting solar cell. The double-junction solar cell with the 801 nm spectral splitting with an active area of 0.18 cm^2 was found to work with a PCE of 25.3%, which is the highest reported so far for a 4-T all-perovskite double-junction spectral splitting solar cell.

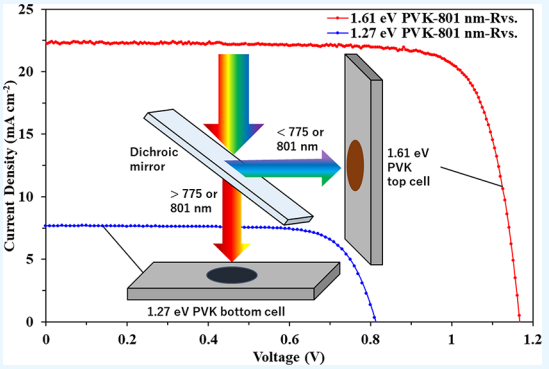

1. INTRODUCTION

Organometal halide perovskite has been attracting huge interests due to its excellent photovoltaic properties such as absorption of light over a wide wavelength range, easily tunable bandgap, and highly efficient photovoltaic conversion.[1−4] In just about a decade, the performance of a single organometal halide perovskite solar cell has been improved to over 25%,[5−7] which is not far from the theoretical efficiency, i.e., a Shockley−Queisser (S−Q) limit of 30%. To achieve a power conversion efficiency (PCE) exceeding this S−Q limit, efforts are made to build a multiple-junction solar of several solar cells with different bandgaps (E_g).[8] The perovskite/perovskite double-junction solar cell has drawn much attention because of its easily tunable bandgap and low-cost fabrication process.[9−14] The perovskite solar cell has three different structures: mesoscopic, planar heterojunction, and inverted.[15,16] Most of the efficient perovskite/perovskite tandem solar cells consist of an inverted structure for the top cell, although a wide-bandgap PSC records a higher PCE with a mesoscopic structure compared to the inverted structure. There were some reports that used a mesoscopic structure for a wide-bandgap PSC, but their reported PCE was around 10% and quite low.[17,18] In this research, more than 25% PCE was obtained using the mesoscopic wide-bandgap perovskite top cell and inverted narrow-bandgap perovskite bottom cell.

Based on their structures, the perovskite/perovskite double-junction solar cells can be divided into two types, two terminals (2-T) and four terminals (4-T).[19] The 2-T solar cells are fabricated by stacking the wide-bandgap top cell and low-bandgap bottom cell with interconnection (recombination) layers.[18,20] In this case, the structure of the top cell (n−i−p or p−i−n) is normally equivalent to that of the bottom cell, and the photocurrent matching must be considered to obtain the best performance, which is not required in the case of 4-T solar cells.[20] This means that, in the 4-T case, the top cell and bottom cell with different structures are fabricated individually and then connected externally through the terminals combining from each subcell—the subcells are optically coupled but electrically independent, which provides more flexibility to the device architecture. Normally, perovskite/perovskite double-junction solar cells consist of top cells made of lead (Pb)-based wide-bandgap perovskites and bottom cells made of tin and lead (Sn−Pb)-based narrow-bandgap perovskites.[21,22] It is well-known that while Pb perovskites work with better PCE in the n−i−p structure,[7,23] the Sn−Pb-based perovskites work with better PCE only in the p−i−n architecture.[24,25] Therefore, theoretically, the use of a Pb-based perovskite cell of the n−i−p structure for the top cell and Sn−Pb-based perovskite cell with

Received: December 3, 2023
Accepted: December 15, 2023
Published: December 29, 2023

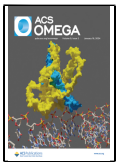

https://doi.org/10.1021/acsomega.3c09654
ACS Omega 2024, 9, 3028−3034

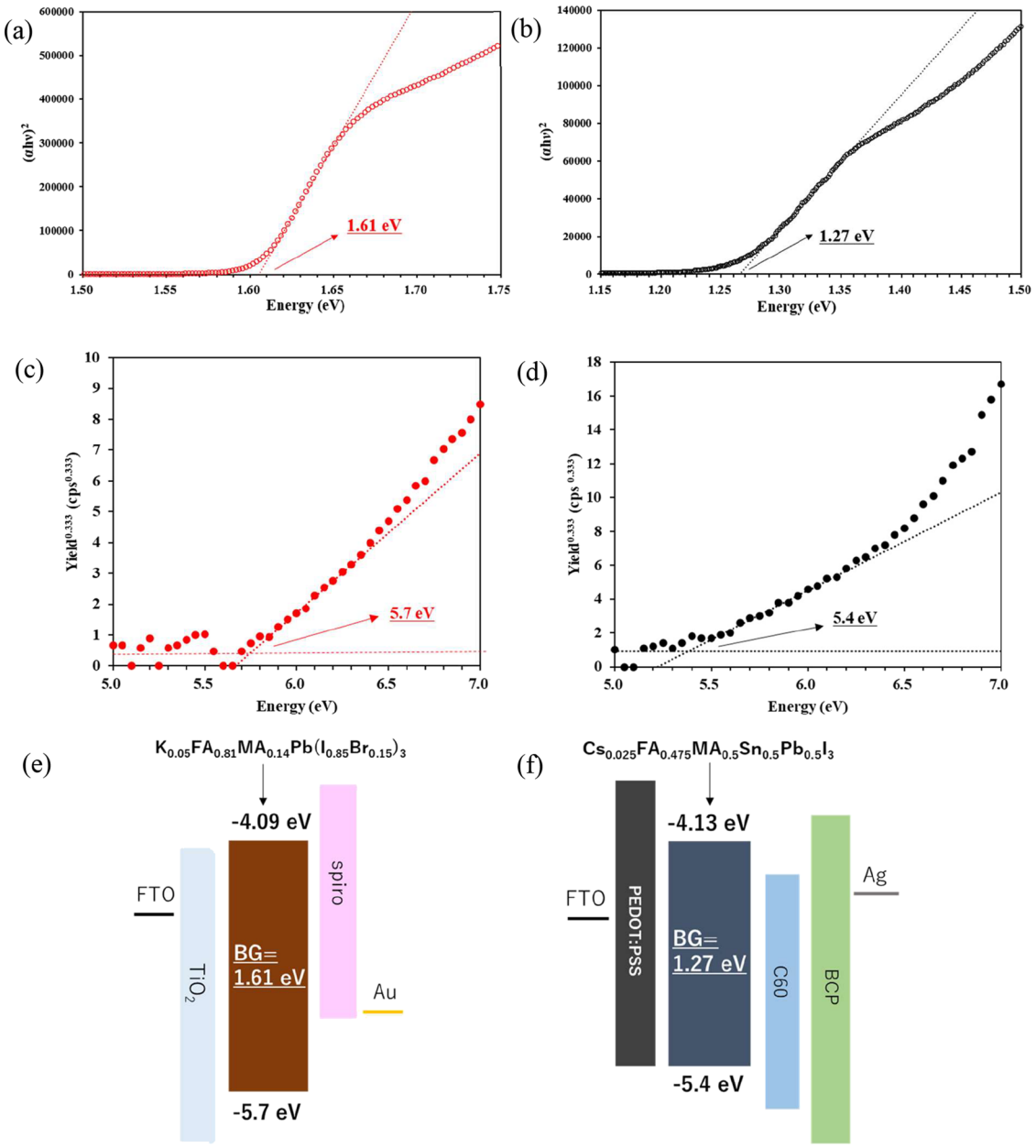

Figure 1. Tauc plot showing the bandgap of PVK with different compositions. (a) $K_{0.05}FA_{0.81}MA_{0.14}Pb(I_{0.85}Br_{0.15})_3$. (b) $Cs_{0.025}FA_{0.475}MA_{0.5}Sn_{0.5}Pb_{0.5}I_3$. Atmospheric photoelectron spectroscopy was used to evaluate the HOMO energy level of PVK with different compositions. (c) $K_{0.05}FA_{0.81}MA_{0.14}Pb(I_{0.85}Br_{0.15})_3$. (d) $Cs_{0.025}FA_{0.475}MA_{0.5}Sn_{0.5}Pb_{0.5}I_3$. Energy-level diagram of PVK with compositions of (e) $K_{0.05}FA_{0.81}MA_{0.14}Pb(I_{0.85}Br_{0.15})_3$ and (f) $Cs_{0.025}FA_{0.475}MA_{0.5}Sn_{0.5}Pb_{0.5}I_3$.

the p−i−n structure for the bottom cell should work with a higher PCE. Moreover, the 4-T double-junction solar cell, compared to 2-T cells, has a wider range of appropriate bandgaps for the top cell and bottom cell.[26,27] However, more than one electrode has to be transparent in the case of a mechanically stacked 4-T cell. Therefore, the use of 4-T solar cells in a spectral splitting system where a dichroic mirror is used to split the incident light selectively for the top cell and bottom cell is an easier and effective method to reduce optical loss and obtain highly efficient double-junction solar cells.[28]

Such a spectral splitting system was first utilized in 1978,[29] and presently, it is applied to the double-junction solar cells.[30−33] Furthermore, there is also ongoing research on spectral splitting systems aimed at practical applications, including their use in electric vehicles.[34] However, there is only one report of the spectral splitting perovskite/perovskite 4-T double-junction solar cell, where the authors fabricated a spectrum-splitting 4-T perovskite solar cell, consisting of a p−i−n Pb PVK top cell and a p−i−n Sn−Pb bottom cell, that showed a PCE of 23.26% with an aperture area of 0.06 cm^2.[35] As the combination of the n−i−p structure Pb PVK top cell and p−i−n structure Sn−Pb PVK bottom cell, which is expected to work better, has not been reported yet, we explored the idea.

In this study, two different types of perovskites were used for an all-perovskite double-junction solar cell. A wide-bandgap Pb perovskite of composition $FA_{0.85}MA_{0.15}Pb(I_{0.85}Br_{0.15})_3$ doped with the 5% potassium ion was fabricated for the top cell. $FAPbI_3$ has been applied to high-efficiency PSCs due to its superior characteristics such as an optimal bandgap, a longer diffusion length, and a high thermal stability.[36,37] Furthermore, the

https://doi.org/10.1021/acsomega.3c09654
ACS Omega 2024, 9, 3028−3034

addition of MABr to $FAPbI_3$ is effective to suppress the transformation of α-phase to δ-phase at room temperature, which is unfavorable for efficient PSCs.[38−40] The reason why the 5% potassium ion was doped into $FA_{0.85}MA_{0.15}Pb(I_{0.85}Br_{0.15})_3$ is the reduction of the hysteresis of PSC, according to the previous report from Tang et al.[41] A Sn−Pb perovskite of composition $Cs_{0.025}FA_{0.475}MA_{0.5}Sn_{0.5}Pb_{0.5}I_3$ with a narrow bandgap that works with a high PCE was chosen for the bottom cell.[42] The detailed fabrication process of each perovskite film is given in the Experimental Methods, and the top-view scanning electron micrographs of the perovskite films are shown in Figure S1.

2. RESULTS AND DISCUSSION

2.1. Energy-Level Characteristics of Wide-Bandgap and Narrow-Bandgap Perovskite Thin Films. The bandgaps of $K_{0.05}FA_{0.81}MA_{0.14}Pb(I_{0.85}Br_{0.15})_3$ (top cell) and $Cs_{0.025}FA_{0.475}MA_{0.5}Sn_{0.5}Pb_{0.5}I_3$ (bottom cell), as confirmed from the Tauc plot (Figure 1a,b), were 1.61 and 1.27 eV, respectively. Atmospheric photoelectron spectroscopy, as shown in Figure 1c,d, was used to determine the HOMO (or valence band) energy level of each perovskite. The ionization potentials that are determined from the point at which the tangent to the yield curve intersects the horizontal baseline (Figure 1 c,d) and that essentially represent the valence band (VB) levels of $K_{0.05}FA_{0.81}MA_{0.14}Pb(I_{0.85}Br_{0.15})_3$ and $Cs_{0.025}FA_{0.475}MA_{0.5}Sn_{0.5}Pb_{0.5}I_3$ were found to be 5.7 and 5.4 eV, respectively. Then, conduction band (CB) levels of both the perovskites were calculated by adding the corresponding bandgap values to their VB levels. The energy-level diagrams of both devices are shown in Figure 1e,f.

2.2. Four-Terminal Spectral Splitting Solar Cells. The top cell with an n−i−p architecture employing the 1.61 eV perovskite (PVK) was fabricated using TiO_2 as the electron transport layer (ETL) and spiro-OMeTAD as the hole transport layer (HTL) and glass/fluorine-doped tin oxide (FTO)/compact titanium oxide (c-TiO_2)/mesoporous titanium oxide (m-TiO_2)/PVK/spiro-OMeTAD/gold (Au) (Figure 2a). The

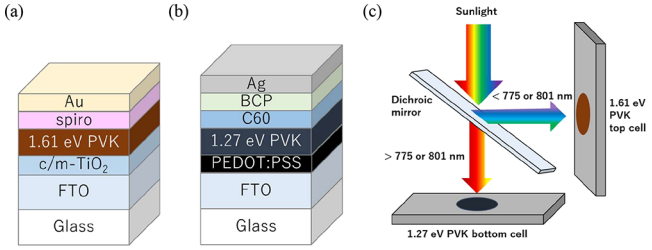

Figure 2. Schemes of fabricated solar cells: (a) 1.61 eV PVK top cell, (b) 1.27 eV PVK bottom cell, and (c) spectral splitting system with a dichroic mirror.

bottom cell including the 1.27 eV PVK was fabricated with a p−i−n architecture and glass/FTO/PEDOT:PSS/PVK/$EDAI_2$/fullerene(C_{60})/bathocuproine (BCP)/silver (Ag) with a 0.18 cm^2 active area (Figure 2b). Here, PEDOT:PSS and C60 were employed as the HTL and ETL, respectively, and $EDAI_2$ surface passivation was applied to suppress the recombination on the perovskite surface.[25] The illumination area for both cells was 0.18 cm^2. The cross-sectional SEM images of each cell are shown in Figure S2. The performance of the fabricated top and bottom cells was measured using a spectral splitting system with a dichroic mirror, which was set at 45° tilted toward both the top and bottom cells, as shown in Figure 2c. Two types of dichroic mirrors were used to determine the PCE of the double-junction 4-T solar cell. The dichroic mirrors of 775 and 801 nm spectral splitting were used because they closely matched the theoretical light absorption edge of PVK in the top cell (1.61 eV), which was approximately 770 nm. In the spectral splitting system, the top cell received the light with wavelengths shorter than 775 or 801 nm, and the bottom cell received the light of wavelengths longer than 775 or 801 nm. The $J-V$ curves of the PVK solar cells, shown in Figure 3, were measured with and without the dichroic

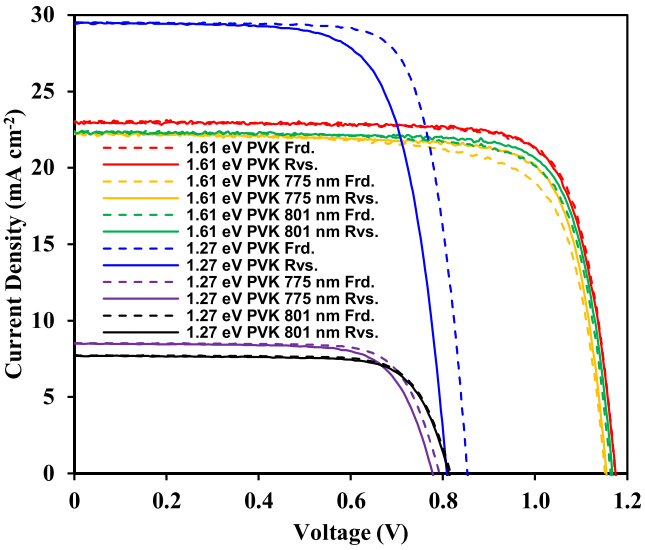

Figure 3. $J-V$ curves of PVK cells in the presence of the dichroic mirror with and without a splitting wavelength of 775 and 801 nm.

mirrors under standard 1 sun illumination. The photovoltaic parameters of the cells are listed in Table 1. Without a dichroic mirror, the PCE (reverse scan) of the top cell was 21.34%, which decreased to 20.65% when a dichroic mirror with a splitting wavelength of 801 nm was used. The decreased PCE is

Table 1. Parameters of the PVK Solar Cells in the Presence of the Dichroic Mirror with and without a Splitting Wavelength of 775 or 801 nm Extracted from $J-V$ Curves

	splitter	scan direction	PCE (%)	J_{SC} (mA/cm^2)	V_{OC} (V)	FF
1.61 eV PVK	W/O	Frd.	21.39	23.03	1.17	0.79
		Rvs	21.34	22.98	1.17	0.79
	775 nm	Frd.	19.12	22.28	1.15	0.71
		Rvs	20.21	22.22	1.15	0.79
	801 nm	Frd.	20.16	22.38	1.16	0.77
		Rvs	20.65	22.37	1.17	0.79
1.27 eV PVK	W/O	Frd.	19.24	29.52	0.85	0.76
		Rvs	17.08	29.44	0.81	0.72
	775 nm	Frd.	5.10	8.53	0.79	0.75
		Rvs	4.87	8.49	0.78	0.74
	801 nm	Frd.	4.80	7.73	0.82	0.76
		Rvs	4.71	7.69	0.81	0.75
4-T tandem	775 nm	Frd.	24.22			
		Rvs	25.08			
	801 nm	Frd.	24.96			
		Rvs	25.36			

https://doi.org/10.1021/acsomega.3c09654
ACS Omega 2024, 9, 3028−3034

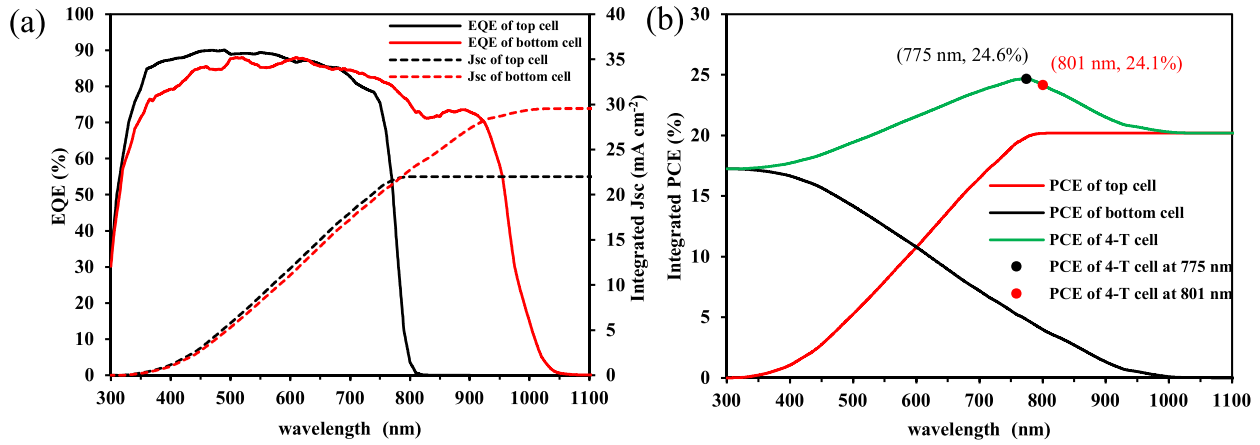

Figure 4. (a) EQE and integrated J_{sc} of PVK solar cells with 1.61 and 1.27 eV and the pictures of the top and bottom PVK cells. (b) Integrated PCE of the top, bottom, and 4-T tandem solar cells.

reasonable because the dichroic mirror slightly reduces the intensity of reaching the top cell, resulting in a slight reduction in short-circuit current density (J_{sc}) from 22.98 to 22.37 mA cm^{-2}, while the open circuit voltage (V_{oc}) (1.17 V) and fill factor (FF) (0.77) remained unchanged. Compared to this result, the PCE (reverse scan) of the top cell with a splitting wavelength of 775 nm was measured to be lower, 20.21% with a J_{sc} of 22.22 mA cm^{-2}, a V_{oc} of 1.15 V, and an FF of 0.79. For the bottom cell, the PCE measured on a reverse scan, with a splitting wavelength of 775 nm, was 4.87% PCE, which was higher than the PCE (4.71%) obtained with an 801 nm spectral splitting. However, the difference in PCEs obtained with 775 and 801 nm dichroic mirrors for the bottom cell was 0.16%, which was smaller than the difference measured for the top cell. Eventually, the best PCE of 25.36% for the double-junction 4-T spectral splitting solar cell composed of a 1.61 eV PVK top cell and a 1.27 eV PVK bottom cell was achieved with a splitting wavelength of 801 nm.

The external quantum efficiency (EQE) spectra acquired for the top and bottom cells without a dichroic mirror are shown in Figure 4a. As can be seen in Figure 4a, the edge of the light absorption of the top PVK cell is around 800 nm and that of the bottom cell is around 1050 nm. Furthermore, the J_{sc} values of the top and bottom cells were derived from the EQE spectrum to be 22.02 and 29.56 mA cm^{-2}, respectively. The integrated J_{sc} of the bottom cell matches the measured value of J_{sc} (29.44 mA cm^2) in Table 1. The calculated J_{sc} of the top cell was approximately 1.0 mA cm^{-2} less than the actual measured J_{sc}. The integrated PCE of the top and bottom cells was also derived from the multiplication of J_{sc}, calculated from the EQE spectrum, and measured V_{oc} (1.17 and 0.81 V) and FF (0.79 and 0.72) from Table 1, while the V_{oc} and FF were assumed to be the same (Figure 4b). The integrated PCE of the 4-T tandem solar cell was derived by adding a PCE of the top cell, integrated from the smaller wavelengths, and a PCE of the bottom cell, integrated from the longer wavelengths. As shown in Figure 4b, the derived PCE at the 775 nm split was 24.6%, and the derived PCE of the 801 nm split was 24.1%. The results show that the use of the 775 and 801 nm spectrum splitter was ideal to obtain an efficient PCE in the case of the spectrum-splitting tandem solar cell including the 1.61 eV PVK solar cell and 1.27 eV PVK solar cell.

3. CONCLUSIONS

In conclusion, a spectral splitting double-junction 4-T solar cell with a 1.61 eV PVK top cell with a mesoscopic (n−i−p) structure and a 1.27 eV PVK bottom cell with an inverted (p−i−n) structure was fabricated. By applying a dichroic mirror with an 801 nm splitting wavelength to the double-junction solar cell, a PCE of 25.3% was obtained, which was the highest PCE reported for a perovskite/perovskite spectral splitting solar cell. This study also revealed that such a spectral splitting system was an uncomplicated but efficient method for obtaining a highly efficient all-perovskite double-junction solar cell because the top cell and bottom cell can be fabricated individually, and the best wavelength for spectral splitting can be easily adjusted. In addition, this research demonstrates the importance of combining the Pb PVK solar cell with the n−i−p structure and the Sn−Pb PVK solar cell with the p−i−n structure to fabricate a more efficient perovskite/perovskite double-junction solar cell. For increasing the PCE of such perovskite/perovskite double-junction solar cells further, the performance of the narrow-bandgap bottom cell needs to be improved, which can be achieved by widening the optical absorption further.

4. EXPERIMENTAL METHODS

4.1. Materials. All of the chemicals and solvents were used without any purification. For the preparation of K 5% doped $FA_{0.85}MA_{0.15}Pb(I_{0.85}Br_{0.15})_3$ perovskite solar cell fabrication, $PbBr_2$ (>99.99%) was purchased from Alfa Aesar. MABr (methylammonium bromide) (>99%) was purchased from Dyesol Ltd. Acetonitrile (super dehydrated), 2-propnaol (super dehydrated), DMF (*N*,*N*-dimethylformamide), and DMSO (dimethyl sulfoxide) were purchased from FUJIFILM Wako Pure Chemical Corporation. PST-18NR was purchased from JGS Catalysts and Chemicals Ltd. Ethanol (>99%) and acetone (>99%) were purchased from Nacalai Tesque, Inc. Spiro-OMeTAD (>99.97%) was purchased from Nippon Fine Chemical Co., Ltd. Titanium diisopropoxide bis-(acetylacetonate) (75 wt % in isopropanol) was purchased from Sigma-Aldrich. FAI (formamidinium iodide) (99.99%), KI (>99.5%), LiTFSI (lithium bis(trifluoromethanesulfonyl)-imide), $Mg(TFSI)_2$ (magnesium(II) bis-(trifluoromethanesulfonyl)imide), PbI_2 (99.99%), and tBP (4-*tert*-butylpyridine) were purchased from TCI (Tokyo Chemical Industry) Co., Ltd. For the preparation of $Cs_{0.025}FA_{0.475}MA_{0.5}Sn_{0.5}Pb_{0.5}I_3$ perovskite solar cell fabrication, 2-propnal (super dehydrated, 99.7%) was purchased from FUJIFILM Wako Pure Chemical Corporation. PEDOT:PSS was purchased from Heraeus. Silver (99.999%) and SnF_2

https://doi.org/10.1021/acsomega.3c09654
ACS Omega 2024, 9, 3028−3034

(100%) were purchased from Kojundo Chemical Laboratory Co., Ltd. 2-Propnaol (>99%) and acetone (>99%) were purchased from Nacalai Tesque, Inc. C60 was purchased from Nanom Purple SC. BCP (bathocuproine) (99.99%), CsI (99.999%), DMF (*N*,*N*-dimethylformamide) (99.8%), DMSO (dimethyl sulfoxide) (99.9%), GlyHCl (glycine hydrochloride) (>99%), $Pb(SCN)_2$ (99.5%), PbI_2 (99.999%), SnI_2 (99.99%), and toluene were purchased from Sigma-Aldrich. $EDAI_2$ (ethylenediamine dihydroiodide) (>98.0%), FAI (98%), and MAI (99%) were purchased from TCI Co., Ltd.

4.2. Fabrication of the 1.61 eV Wide-Bandgap Perovskite Solar Cell. First, the fluorine-doped tin oxide (FTO) substrate with a 10 Ω/equiv resistance was cleaned by ultrasonication in acetone and ethanol for 10 min each. Afterward, the FTO substrate was treated with UV-ozone for 10 min, and the compact TiO_2 layer was fabricated by spray coating on the FTO substrate at 430 °C using titanium diisopropoxide bis(acetylacetonate) dissolved in ethanol precursor solution including LiTFSI and $Mg(TFSI)_2$. Subsequently, 2 wt % TiO_2 (PST-18NR) solved in ethanol solution was spin-coated on the compact TiO_2 layer and sintered at 430 °C for 30 min to fabricate the mesoporous TiO_2 layer. Additionally, 0.1 M LiTFSI solution dissolved in acetonitrile was spin-coated on the mesoporous TiO_2 layer and sintered at 450 °C for 30 min as Li-doping. The K-doped $FA_{0.85}MA_{0.15}Pb(I_{0.85}Br_{0.15})_3$ perovskite layer was fabricated through the antisolvent process. At first, 1.15 mmol of PbI_2, 0.20 mmol of $PbBr_2$, 1.09 mmol of FAI, and 0.20 mmol of MABr were dissolved in 1 mL of DMF and DMSO mixed solution (4:1, v/v), and apart from that, 1.5 M KI solution was prepared by dissolving in DMSO, and it was added to the base solution with a 5% volume ratio. Perovskite precursor solution was dropped on the substrate and spin-coated at 1000 rpm for 10 s and 4000 rpm for 30 s. During the spin-coating process, 0.8 mL of chlorobenzene was quickly dropped 10 s before the end of the spin-coating process. Then, the substrate was annealed at 160 °C for 15 min. The HTL precursor solution was prepared by mixing 72.3 mg/mL spiro-OMeTAD in chlorobenzene, 28.8 μL of tBP, and 17.5 μL of LiTFSI solution (520 mg of LiTFSI dissolved in 1 mL of acetonitrile). The prepared HTL solution was spin-coated on the perovskite layer at 4000 rpm for 30 s. Finally, the gold electrode (∼100 nm) was thermally evaporated on the HTL layer. The fabricated top cell was stored in 4 days under 20% relative humidity for aging, and the AR (antireflecting) coating seal was placed on the top of the glass substrate.

4.3. Fabrication of the 1.27 eV Narrow-Bandgap Perovskite Solar Cell. Preparation and cleaning of FTO substrates were the same as previously described in the top cell fabrication. First, PEDOT:PSS solution was filtered through a 0.2 μm PTFE filter and spun on the FTO substrate at 4000 rpm for 50 s. Afterward, the FTO substrate was annealed on a hot plate at 175 °C for 20 min. Subsequently, the FTO substrate with the HTL was transferred into the glovebox. Before the fabrication of the perovskite layer, the substrate was annealed at 140 °C for 20 min. For the preparation of narrow-bandgap perovskite precursor solution, 1.2 M $Cs_{0.05}FA_{0.95}SnI_3$ solution was prepared by mixing 1.14 mmol of FAI, 1.2 mmol of SnI_2, 0.15 mmol of SnF_2, 0.06 mmol of CsI, and 20 mg of Sn (metal) in 1 mL of DMF and DMSO solution (8:2, v/v). In different vials, 1.2 M $MAPbI_3$ solution was prepared by dissolving 1.2 mmol of MAI, 1.2 mmol of PbI_2, and 0.04 mmol of $Pb(SCN)_2$ into 1 mL of DMF and DMSO solution (8:2, v/v). Both vials were preheated at 70 °C for 2 h inside the glovebox before the usage. Next, 1.2 M $Cs_{0.025}FA_{0.475}MA_{0.5}Sn_{0.5}Pb_{0.5}I_3$ precursor solution was obtained by stoichiometrically combining $Cs_{0.05}FA_{0.95}SnI_3$ and $MAPbI_3$ solution and filtering with a 0.2 μm PTFE filter. Finally, GlyHCl was added to the precursor solution with a ratio of 2 mol % and dissolved. After the substrate was cooled to room temperature, 100 μL of perovskite precursor solution was dropped on the substrate and spin-coated at 3000 rpm for 10 s, followed by 5000 rpm for 50 s. During the spin-coating process, 400 μL of toluene was dropped quickly on the substrate, and then annealing at 100 °C for 1 min was performed to fabricate the Sn−Pb perovskite layer. Afterward, the perovskite layer was passivated by spin-coating 0.2 μm PTFE filtered $EDAI_2$ solution (0.5 mM in 2-propanol (super dehydrated) and toluene, 1:1, v/v) at 4000 rpm for 20 s. Continuously, the solution was dried at 100 °C for 5 min. Finally, the substrate was transferred to the evaporator, and C60 (20 nm), BCP (5 nm), and Ag (80 nm) were thermally evaporated under high vacuum conditions.

4.4. Characterization. To ascertain the bandgap of each perovskite, a UV−vis−NIR spectrophotometer (UV-3600, Shimadzu, Japan) was employed to derive the Tauc plot. Consequently, the thickness of the perovskite thin film was determined by using a step gauge (Surfcorder ET-4000A, Kosaka Laboratory Ltd., Japan). Detailed information regarding the calculation methodology is available in the Supporting Information. The energy level of the perovskite's valence band was ascertained by measuring the ionization potential of the perovskite thin layer using an atmospheric photoelectron spectrometer (AC-3, Rikenkeiki, Japan). During the measurement, the light intensity was set at 7 nW and the power multiplier was adjusted to 1/3. The energy range covered in the measurement extended from 4.00 to 7.00 eV, with the measurement taken at intervals of 0.05 eV. The surface morphology of the perovskite thin films and cross-sectional image of perovskite solar cells were examined using a scanning electron microscope (FE-SEM SU8000, Hitachi High-Tech, Japan). The electron beam was operated at an accelerated voltage of 10 kV and a current of 10 μA. Current density−voltage (*J*−*V*) were conducted in both forward and reverse scans using a solar simulator (Keithley model 2401 and Modulab) under 100 mW cm^{-2}, AM 1.5G illumination (YSS-80A, Yamashita Denso, Japan) in a dry room with humidity levels maintained below 500 rpm. In the forward scan, the voltage was swept from −0.2 to 1.2 V, and the reverse scan covered the range from 1.2 to −0.2 V with a step size of 100 mV. To ensure the accuracy of incident power, the short circuit current of a Si photodiode detector (BS-520BK, Bunkoukeiki, Japan) was initially measured at the beginning of the experiment. The active area of the perovskite solar cell, which was 0.18 cm^2 in size, was defined using an optical mask, and dichroic mirrors (Semrock) were utilized for spectral splitting. The EQE spectra were acquired in the wavelength range of 300 to 1200 nm using a CEP-2000MLQ instrument. These measurements were conducted under the illumination source BPS-X300B (Bunkoukeiki, Japan), with a light intensity of 0.2×10^{-16} photons.

■ ASSOCIATED CONTENT

Supporting Information

The Supporting Information is available free of charge at https://pubs.acs.org/doi/10.1021/acsomega.3c09654.

https://doi.org/10.1021/acsomega.3c09654
ACS Omega 2024, 9, 3028−3034

Description of characterization methods, SEM, and photographs of the spectrum-splitting system and cell holder for the $J-V$ measurement (PDF)

AUTHOR INFORMATION

Corresponding Authors

Satoshi Uchida − *Research Center for Advanced Science and Technology (RCAST), The University of Tokyo, Tokyo 153-8904, Japan;* orcid.org/0000-0002-4971-574X; Email: uchida@rcast.u-tokyo.ac.jp

Hiroshi Segawa − *Department of Chemical System Engineering, Graduate School of Engineering, The University of Tokyo, Tokyo 113-8656, Japan; Department of General Systems Studies, Graduate School of Arts and Sciences, The University of Tokyo, Tokyo 153-8902, Japan; Research Center for Advanced Science and Technology (RCAST), The University of Tokyo, Tokyo 153-8904, Japan;* orcid.org/0000-0001-8076-9722; Email: csegawa@mail.ecc.u-tokyo.ac.jp

Authors

Kei Ito − *Department of Chemical System Engineering, Graduate School of Engineering, The University of Tokyo, Tokyo 113-8656, Japan*

Kazuteru Nonomura − *Department of General Systems Studies, Graduate School of Arts and Sciences, The University of Tokyo, Tokyo 153-8902, Japan*

Ryota Kan − *Department of General Systems Studies, Graduate School of Arts and Sciences, The University of Tokyo, Tokyo 153-8902, Japan*

Keishi Tada − *Department of General Systems Studies, Graduate School of Arts and Sciences, The University of Tokyo, Tokyo 153-8902, Japan;* orcid.org/0000-0002-3014-2515

Ching Chang Lin − *Department of General Systems Studies, Graduate School of Arts and Sciences, The University of Tokyo, Tokyo 153-8902, Japan;* orcid.org/0000-0003-0970-3071

Takumi Kinoshita − *Department of General Systems Studies, Graduate School of Arts and Sciences, The University of Tokyo, Tokyo 153-8902, Japan;* orcid.org/0000-0003-4822-9966

Takeru Bessho − *Research Center for Advanced Science and Technology (RCAST), The University of Tokyo, Tokyo 153-8904, Japan;* orcid.org/0000-0002-3473-2950

Complete contact information is available at: https://pubs.acs.org/10.1021/acsomega.3c09654

Notes

The authors declare no competing financial interest.

ACKNOWLEDGMENTS

This paper is based on the results obtained from a project commissioned by the New Energy and Industrial Technology Development Organization (NEDO, Japan).

REFERENCES

(1) Lee, M. M.; Teuscher, J.; Miyasaka, T.; Murakami, T. N.; Snaith, H. J. Efficient Hybrid Solar Cells Based on Meso-Superstructured Organometal Halide Perovskites. *Science* **2012**, *338* (6107), 643−647.

(2) Kim, H. S.; Lee, C. R.; Im, J. H.; Lee, K. B.; Moehl, T.; Marchioro, A.; Moon, S. J.; Humphry-Baker, R.; Yum, J. H.; Moser, J. E.; Grätzel, M.; Park, N. G. Lead Iodide Perovskite Sensitized All-Solid-State Submicron Thin Film Mesoscopic Solar Cell with Efficiency Exceeding 9%. *Sci. Rep.* **2012**, *2* (1), 591.

(3) Heo, J. H.; Im, S. H.; Noh, J. H.; Mandal, T. N.; Lim, C. S.; Chang, J. A.; Lee, Y. H.; Kim, H. J.; Sarkar, A.; Nazeeruddin, M. K.; Grätzel, M.; Seok, S. Il. Efficient Inorganic-Organic Hybrid Heterojunction Solar Cells Containing Perovskite Compound and Polymeric Hole Conductors. *Nat. Photonics* **2013**, *7* (6), 486−491.

(4) Stoumpos, C. C.; Malliakas, C. D.; Kanatzidis, M. G. Semiconducting Tin and Lead Iodide Perovskites with Organic Cations: Phase Transitions, High Mobilities, and near-Infrared Photoluminescent Properties. *Inorg. Chem.* **2013**, *52* (15), 9019−9038.

(5) Zhao, Y.; Ma, F.; Qu, Z.; Yu, S.; Shen, T.; Deng, H. X.; Chu, X.; Peng, X.; Yuan, Y.; Zhang, X.; You, J. Inactive $(PbI_2)_2RbCl$ Stabilizes Perovskite Films for Efficient Solar Cells. *Science (80-.)* **2022**, *377* (6605), 531−534.

(6) Jeong, M. J.; Moon, C. S.; Lee, S.; Im, J. M.; Woo, M. Y.; Lee, J. H.; Cho, H.; Jeon, S. W.; Noh, J. H. Boosting Radiation of Stacked Halide Layer for Perovskite Solar Cells with Efficiency over 25%. *Joule* **2023**, *7* (1), 112−127.

(7) Park, J.; Kim, J.; Yun, H.-S.; Paik, M. J.; Noh, E.; Mun, H. J.; Kim, M. G.; Shin, T. J.; Seok, S. Il. Controlled Growth of Perovskite Layers with Volatile Alkylammonium Chlorides. *Nature* **2023**, *616* (7958), 724−730.

(8) Torabi, N.; Behjat, A.; Zhou, Y.; Docampo, P.; Stoddard, R. J.; Hillhouse, H. W.; Ameri, T. Progress and Challenges in Perovskite Photovoltaics from Single- to Multi-Junction Cells. *Mater. Today Energy* **2019**, *12*, 70−94.

(9) Eperon, G. E.; Leijtens, T.; Bush, K. A.; Prasanna, R.; Green, T.; Wang, J. T. W.; McMeekin, D. P.; Volonakis, G.; Milot, R. L.; May, R.; Palmstrom, A.; Slotcavage, D. J.; Belisle, R. A.; Patel, J. B.; Parrott, E. S.; Sutton, R. J.; Ma, W.; Moghadam, F.; Conings, B.; Babayigit, A.; Boyen, H. G.; Bent, S.; Giustino, F.; Herz, L. M.; Johnston, M. B.; McGehee, M. D.; Snaith, H. J. Perovskite-Perovskite Tandem Photovoltaics with Optimized Band Gaps. *Science.* **2016**, *354* (6314), 861−865.

(10) Jiang, Q.; Tong, J.; Scheidt, R. A.; Wang, X.; Louks, A. E.; Xian, Y.; Tirawat, R.; Palmstrom, A. F.; Hautzinger, M. P.; Harvey, S. P.; Johnston, S.; Schelhas, L. T.; Larson, B. W.; Warren, E. L.; Beard, M. C.; Berry, J. J.; Yan, Y.; Zhu, K. Compositional Texture Engineering for Highly Stable Wide-Bandgap Perovskite Solar Cells. *Science.* **2022**, *378* (6626), 1295−1300.

(11) He, R.; Yi, Z.; Luo, Y.; Luo, J.; Wei, Q.; Lai, H.; Huang, H.; Zou, B.; Cui, G.; Wang, W.; Xiao, C.; Ren, S.; Chen, C.; Wang, C.; Xing, G.; Fu, F.; Zhao, D. Pure 2D Perovskite Formation by Interfacial Engineering Yields a High Open-Circuit Voltage beyond 1.28 V for 1.77-EV Wide-Bandgap Perovskite Solar Cells. *Adv. Sci.* **2022**, *9* (36), 1−11.

(12) Hu, X.; Li, J.; Wang, C.; Cui, H.; Liu, Y.; Zhou, S.; Guan, H.; Ke, W.; Tao, C.; Fang, G. Antimony Potassium Tartrate Stabilizes Wide-Bandgap Perovskites for Inverted 4-T All-Perovskite Tandem Solar Cells with Efficiencies over 26%. *Nano-Micro Lett.* **2023**, *15* (1), 103.

(13) Bi, H.; Fujiwara, Y.; Kapil, G.; Tavgeniene, D.; Zhang, Z.; Wang, L.; Ding, C.; Sahamir, S. R.; Baranwal, A. K.; Sanehira, Y.; Takeshi, K.; Shi, G.; Bessho, T.; Segawa, H.; Grigalevicius, S.; Shen, Q.; Hayase, S. Perovskite Solar Cells Consisting of PTAA Modified with Monomolecular Layer and Application to All-Perovskite Tandem Solar Cells with Efficiency over 25%. *Adv. Funct. Mater.* **2023**, *33* (32), No. 2300089.

(14) Lin, R.; Wang, Y.; Lu, Q.; Tang, B.; Li, J.; Gao, H.; Gao, Y.; Li, H.; Ding, C.; Wen, J.; Wu, P.; Liu, C.; Zhao, S.; Xiao, K.; Liu, Z.; Ma, C.; Deng, Y.; Li, L.; Fan, F.; Tan, H. All-Perovskite Tandem Solar Cells with 3D/3D Bilayer Perovskite Heterojunction. *Nature* **2023**, *620*, 994−1000.

(15) Nakazaki, J.; Segawa, H. Evolution of Organometal Halide Solar Cells. *J. Photochem. Photobiol. C Photochem. Rev.* **2018**, *35*, 74−107.

(16) Park, N. G.; Segawa, H. Research Direction toward Theoretical Efficiency in Perovskite Solar Cells. *ACS Photonics* **2018**, *5* (8), 2970−2977.

(17) Heo, J. H.; Im, S. H. $CH_3NH_3PbBr_3$−$CH_3NH_3PbI_3$Perovskite−Perovskite Tandem Solar Cells with Exceeding 2.2 V Open Circuit Voltage. *Adv. Mater.* **2016**, *28* (25), 5121−5125.
(18) Jiang, F.; Liu, T.; Luo, B.; Tong, J.; Qin, F.; Xiong, S.; Li, Z.; Zhou, Y. A Two-Terminal Perovskite/Perovskite Tandem Solar Cell. *J. Mater. Chem. A* **2016**, *4* (4), 1208−1213.
(19) Todorov, T.; Gunawan, O.; Guha, S. A Road towards 25% Efficiency and beyond: Perovskite Tandem Solar Cells. *Mol. Syst. Des. Eng.* **2016**, *1* (4), 370−376.
(20) He, R.; Ren, S.; Chen, C.; Yi, Z.; Luo, Y.; Lai, H.; Wang, W.; Zeng, G.; Hao, X.; Wang, Y.; Zhang, J.; Wang, C.; Wu, L.; Fu, F.; Zhao, D. Wide-Bandgap Organic-Inorganic Hybrid and All-Inorganic Perovskite Solar Cells and Their Application in All-Perovskite Tandem Solar Cells. *Energy Environ. Sci.* **2021**, *14* (11), 5723−5759.
(21) Zheng, X.; Alsalloum, A. Y.; Hou, Y.; Sargent, E. H.; Bakr, O. M. All-Perovskite Tandem Solar Cells: A Roadmap to Uniting High Efficiency with High Stability. *Accounts Mater. Res.* **2020**, *1* (1), 63−76.
(22) Chen, H.; Maxwell, A.; Li, C.; Teale, S.; Chen, B.; Zhu, T.; Ugur, E.; Harrison, G.; Grater, L.; Wang, J.; Wang, Z.; Zeng, L.; Park, S. M.; Chen, L.; Serles, P.; Awni, R. A.; Subedi, B.; Zheng, X.; Xiao, C.; Podraza, N. J.; Filleter, T.; Liu, C.; Yang, Y.; Luther, J. M.; De Wolf, S.; Kanatzidis, M. G.; Yan, Y.; Sargent, E. H. Regulating Surface Potential Maximizes Voltage in All-Perovskite Tandems. *Nature* **2023**, *613* (7945), 676−681.
(23) Jeong, J.; Kim, M.; Seo, J.; Lu, H.; Ahlawat, P.; Mishra, A.; Yang, Y.; Hope, M. A.; Eickemeyer, F. T.; Kim, M.; Yoon, Y. J.; Choi, I. W.; Darwich, B. P.; Choi, S. J.; Jo, Y.; Lee, J. H.; Walker, B.; Zakeeruddin, S. M.; Emsley, L.; Rothlisberger, U.; Hagfeldt, A.; Kim, D. S.; Grätzel, M.; Kim, J. Y. Pseudo-Halide Anion Engineering for α-FAPbI3 Perovskite Solar Cells. *Nature* **2021**, *592* (7854), 381−385.
(24) Kapil, G.; Bessho, T.; Sanehira, Y.; Sahamir, S. R.; Chen, M.; Baranwal, A. K.; Liu, D.; Sono, Y.; Hirotani, D.; Nomura, D.; Nishimura, K.; Kamarudin, M. A.; Shen, Q.; Segawa, H.; Hayase, S. Tin-Lead Perovskite Solar Cells Fabricated on Hole Selective Monolayers. *ACS Energy Lett.* **2022**, *7* (3), 966−974.
(25) Hu, S.; Otsuka, K.; Murdey, R.; Nakamura, T.; Truong, M. A.; Yamada, T.; Handa, T.; Matsuda, K.; Nakano, K.; Sato, A.; Marumoto, K.; Tajima, K.; Kanemitsu, Y.; Wakamiya, A. Optimized Carrier Extraction at Interfaces for 23.6% Efficient Tin-Lead Perovskite Solar Cells. *Energy Environ. Sci.* **2022**, *15* (5), 2096−2107.
(26) Eperon, G. E.; Hörantner, M. T.; Snaith, H. J. Metal Halide Perovskite Tandem and Multiple-Junction Photovoltaics. *Nat. Rev. Chem.* **2017**, *1* (12), No. 0095.
(27) Leijtens, T.; Bush, K. A.; Prasanna, R.; McGehee, M. D. Opportunities and Challenges for Tandem Solar Cells Using Metal Halide Perovskite Semiconductors. *Nat. Energy* **2018**, *3* (10), 828−838.
(28) Crisostomo, F.; Taylor, R. A.; Surjadi, D.; Mojiri, A.; Rosengarten, G.; Hawkes, E. R. Spectral Splitting Strategy and Optical Model for the Development of a Concentrating Hybrid PV/T Collector. *Appl. Energy* **2015**, *141*, 238−246.
(29) Green, M. A.; Ho-Baillie, A. Forty Three per Cent Composite Split-Spectrum Concentrator Solar Cell Efficiency. *Prog. Photovoltaics Res. Appl.* **2010**, *18* (1), 42−47.
(30) Kinoshita, T.; Nonomura, K.; Joong Jeon, N.; Giordano, F.; Abate, A.; Uchida, S.; Kubo, T.; Seok, S. I.; Nazeeruddin, M. K.; Hagfeldt, A.; Grätzel, M.; Segawa, H. Spectral Splitting Photovoltaics Using Perovskite and Wideband Dye-Sensitized Solar Cells. *Nat. Commun.* **2015**, *6* (1), 8834.
(31) Duong, T.; Grant, D.; Rahman, S.; Blakers, A.; Weber, K. J.; Catchpole, K. R.; White, T. P. Filterless Spectral Splitting Perovskite-Silicon Tandem System with > 23% Calculated Efficiency. *IEEE J. Photovoltaics* **2016**, *6* (6), 1432−1439.
(32) Nakamura, M.; Tada, K.; Kinoshita, T.; Bessho, T.; Nishiyama, C.; Takenaka, I.; Kimoto, Y.; Higashino, Y.; Sugimoto, H.; Segawa, H. Perovskite/CIGS Spectral Splitting Double Junction Solar Cell with 28% Power Conversion Efficiency. *iScience* **2020**, *23* (12), No. 101817.
(33) Feeney, T.; Hossain, I. M.; Gharibzadeh, S.; Gota, F.; Singh, R.; Fassl, P.; Mertens, A.; Farag, A.; Becker, J. P.; Paetel, S.; Ahlswede, E.; Paetzold, U. W. Four-Terminal Perovskite/Copper Indium Gallium Selenide Tandem Solar Cells: Unveiling the Path to > 27% in Power Conversion Efficiency. *Sol. RRL* **2022**, *6* (12), No. 2200662.
(34) Vu, N. H.; Pham, T. T.; Shin, S. Flat Concentrator Photovoltaic System for Automotive Applications. *Sol. Energy* **2019**, *190*, 246−254.
(35) Yao, Y.; Lv, F.; Luo, L.; Liao, L.; Wang, G.; Liu, D.; Xu, C.; Zhou, G.; Zhao, X.; Song, Q. Highly Efficient Sn−Pb Perovskite Solar Cell and High-Performance All-Perovskite Four-Terminal Tandem Solar Cell. *Sol. RRL* **2020**, *4* (3), 1−7.
(36) Eperon, G. E.; Stranks, S. D.; Menelaou, C.; Johnston, M. B.; Herz, L. M.; Snaith, H. J. Formamidinium Lead Trihalide: A Broadly Tunable Perovskite for Efficient Planar Heterojunction Solar Cells. *Energy Environ. Sci.* **2014**, *7* (3), 982−988.
(37) Yang, S.; Liu, Y.; Lian, X.; Chu, J. Inactive Impurity Stabilizes the Highly Efficient Perovskite Photovoltaics. *Joule* **2022**, *6* (10), 2248−2250.
(38) Jeon, N. J.; Noh, J. H.; Yang, W. S.; Kim, Y. C.; Ryu, S.; Seo, J.; Seok, S. Il. Compositional Engineering of Perovskite Materials for High-Performance Solar Cells. *Nature* **2015**, *517* (7535), 476−480.
(39) Zheng, X.; Wu, C.; Jha, S. K.; Li, Z.; Zhu, K.; Priya, S. Improved Phase Stability of Formamidinium Lead Triiodide Perovskite by Strain Relaxation. *ACS Energy Lett.* **2016**, *1* (5), 1014−1020.
(40) Ruellou, J.; Courty, M.; Sauvage, F. Thermal and Photo-Degradation Study of α-$FAPbI_3$-Based Perovskite Using In Situ X-Ray Diffraction. *Adv. Funct. Mater.* **2023**, *33* (34), No. 2300811.
(41) Tang, Z.; Bessho, T.; Awai, F.; Kinoshita, T.; Maitani, M. M.; Jono, R.; Murakami, T. N.; Wang, H.; Kubo, T.; Uchida, S.; Segawa, H. Hysteresis-Free Perovskite Solar Cells Made of Potassium-Doped Organometal Halide Perovskite. *Sci. Rep.* **2017**, *7* (1), 1−7.
(42) Kapil, G.; Bessho, T.; Maekawa, T.; Baranwal, A. K.; Zhang, Y.; Kamarudin, M. A.; Hirotani, D.; Shen, Q.; Segawa, H.; Hayase, S. Tin-Lead Perovskite Fabricated via Ethylenediamine Interlayer Guides to the Solar Cell Efficiency of 21.74%. *Adv. Energy Mater.* **2021**, *11* (25), 2−4.

https://doi.org/10.1021/acsomega.3c09654
ACS Omega 2024, 9, 3028−3034